Journal of Power Sources 243 (2013) 290–298

Contents lists available at SciVerse ScienceDirect

Journal of Power Sources

journal homepage: www.elsevier.com/locate/jpowsour

Comparing aging of graphite/$LiFePO_4$ cells at 22 °C and 55 °C – Electrochemical and photoelectron spectroscopy studies

Maria Hellqvist Kjell [a,*], Sara Malmgren [b], Katarzyna Ciosek [b], Mårten Behm [a], Kristina Edström [b], Göran Lindbergh [a]

[a] School of Chemical Science and Engineering, Department of Chemical Engineering and Technology, Applied Electrochemistry, KTH Royal Institute of Technology, SE-100 44 Stockholm, Sweden
[b] Department of Chemistry Ångström Laboratory, Uppsala University, Box 538, SE-751 21 Uppsala, Sweden

HIGHLIGHTS

- Comparing aging of graphite/$LiFePO_4$-based cells at 22 °C and 55 °C.
- Cycle-aging using a synthetic hybrid drive cycle.
- 22 °C and 55 °C cells show, e.g., different capacity loss and impedance at EOL.
- XPS spectra of electrodes cycle aged at the same temperature were similar.
- Degradation processes are accelerated in process specific ways.

ARTICLE INFO

Article history:
Received 26 March 2013
Received in revised form
30 May 2013
Accepted 3 June 2013
Available online 11 June 2013

Keywords:
Aging
XPS
$LiFePO_4$
Electrolyte degradation
Lithium-ion battery

ABSTRACT

Accelerated aging at elevated temperature is commonly used to test lithium-ion battery lifetime, but the effect of an elevated temperature is still not well understood. If aging at elevated temperature would only be faster, but in all other respects equivalent to aging at ambient temperature, cells aged to end-of-life (EOL) at different temperatures would be very similar. The present study compares graphite/$LiFePO_4$-based cells either cycle- or calendar-aged to EOL at 22 °C and 55 °C. Cells cycled at the two temperatures show differences in electrochemical impedance spectra as well as in X-ray photoelectron spectroscopy (XPS) spectra. These results show that lithium-ion cell aging is a complex set of processes. At elevated temperature, the aging is accelerated in process-specific ways. Furthermore, the XPS results of cycle-aged samples indicate increased deposition of oxygenated $LiPF_6$ decomposition products in both the negative and positive electrode/electrolyte interfaces. The decomposition seems more pronounced at elevated temperature, and largely accelerated by cycling, which could contribute to the observed cell impedance increase.

© 2013 Elsevier B.V. All rights reserved.

1. Introduction

Lithium-ion batteries, including graphite/$LiFePO_4$-based ones, are attractive for energy storage in plug-in and hybrid electric vehicles. However, the vehicle lifetime today exceeds the lithium-ion battery lifetime [1]. Therefore, significant efforts are made to estimate and extend the lifetime of various batteries. Accelerated aging at elevated temperature is a commonly employed method to predict battery lifetime at ambient temperature [2]. However, lithium-ion battery aging is a complex set of interacting processes. A range of different aging mechanisms have been proposed for lithium-ion batteries, including the deterioration of the active materials, electrolyte, separator, composite electrode structure, as well as evolution of the solid electrolyte interphase (SEI) [3]. For $LiFePO_4$-based systems, loss of cyclable lithium has been proposed as a major aging mechanism [4–13]. The observed loss of cyclable lithium has been attributed to, e.g., growth of SEI [4,5,7]. Furthermore, the available capacity of $LiFePO_4$ electrodes has been proposed to deteriorate due to, e.g., decreased wettability of the aged electrolyte [14] or particle isolation through cracking [15,16]. Electrolyte degradation may also result in clogging of separator pores [17].

Considering the variety of mechanisms contributing to lithium-ion battery aging, a range of different methods can be used to follow the degradation. Different methods are suitable for

* Corresponding author. Tel.: +46 8 790 81 74.
E-mail address: mariakj@kth.se (M. Hellqvist Kjell).

0378-7753/$ – see front matter © 2013 Elsevier B.V. All rights reserved.
http://dx.doi.org/10.1016/j.jpowsour.2013.06.011

following different processes. For example, the loss of cyclable lithium and increase of impedance can be followed using electrochemical methods such as cycling and electrochemical impedance spectroscopy (EIS). The latter is a commonly used technique to study aging since it is a non-invasive technique where processes of different time scales can be resolved by varying the frequency of an applied potential or current perturbation [18–20]. In general, processes with small time-constants, such as activation polarizations, capacitances, and ohmic resistances, determine the high-frequency semi-circle shape, while the low-frequency tail appearance is governed by large time-constant processes like the mass transport in the active electrode material and electrolyte in Nyquist plots. Therefore, any changes in impedance between beginning-of-life (BOL) and end-of-life (EOL) can be used to follow and identify the origin of aging. Further, three-electrode measurements have successfully been used to separate the different contributions from the positive and negative electrode [21–24].

The electrode/electrolyte interface composition, which is known to change during aging, can be investigated using X-ray photoelectron spectroscopy (XPS). Characterization of electrode/electrolyte interfaces from cycle-aged graphite/$LiFePO_4$ cells by XPS has previously been published by Castro et al. [25]. Interestingly, only a smaller increase in the SEI thickness was observed after cycle aging. However, only washed electrodes were examined with XPS. It is important to study non-washed samples since the solubility of the various SEI compounds and other electrolyte residues deposited onto the particles in the electrodes differ in the organic solvent used to wash samples (generally dimethyl carbonate) [26]. Furthermore, the XPS characterization was performed on electrodes cycled at C/5 or slower for 200 cycles. It is, therefore, interesting to also investigate the electrode/electrolyte interfaces of electrodes aged under more demanding and realistic hybrid drive cycle conditions, and to compare cells at similar states of aging.

In the present work, the methods described above were combined to gain improved insight into the differences between cells cycle-aged to end-of-life at different temperatures, with an emphasis on XPS measurements. If all processes would be accelerated to the same extent at elevated temperature, it could be assumed that batteries cycled to EOL at different temperatures would be very similar in terms of performance, as well as aging-related changes. Discrepancies between cells aged at different temperatures may hence be used to learn more about the relative acceleration of different aging processes at elevated temperature. Such improved insight could facilitate, e.g., more correct estimation of the ambient temperature lifetime based on elevated temperature aging results. The present work compares graphite/$LiFePO_4$ cells cycle- and calendar-aged to EOL at 22 °C and 55 °C with electrochemical methods and XPS. The cycle aging was performed using a synthetic hybrid drive cycle [27]. The results were used to learn more about differences in the aging at different temperatures.

2. Experimental

2.1. Cell assembly

Graphite/$LiFePO_4$ pouch cells (polymer coated aluminum vacuum sealed bags) batteries were assembled using electrodes supplied by Quallion LLC. Table 1 lists the specifications of the electrodes and materials used. All cell components, including the bags with tabs, were dried at 80 °C under reduced pressure over night prior to cell assembly to remove any residual water. Cells were assembled in an argon-filled glove box with inert atmosphere (<1 ppm H_2O). Two-component epoxy glue was applied on the cell edges to minimize water diffusion through the seals, with the additional benefit that the structure of the cells was stabilized to some extent.

Table 1
Cell specifications.

Positive electrode	
Active material	$LiFePO_4$ (Phostech P2)
Active material: binder and carbon	84:16 (wt%)
Current collector/thickness	Aluminum/20 μm
Loading thickness	35 μm
Porosity	27%
Loading density	8 mg cm^{-2}
Negative electrode	
Active material	Graphite
Proportion of active material : binder	90:10 (wt%)
Current collector/thickness	Copper/10 μm
Loading thickness	30 μm
Porosity	45%
Loading density	3.8 mg cm^{-2}
Separator	
Material	PP/PE/PP (Celgard 2320)
Thickness	20 μm
Porosity	39%
Electrolyte	1 M $LiPF_6$ EC:DEC (Merck LP40)

2.2. Electrochemical measurements

Aging experiments were performed at two temperatures: 22 °C and 55 °C. Two different types of aging conditions were investigated: cycle and calendar aging. Before the calendar- and cycle-aging experiments started, the cells were subjected to three consecutive formation cycles at a low rate (C/10; 0.88 A m^{-2}) between 2.5 V and 3.8 V. The cells were then placed in an oil bath at the respective temperature for a minimum of 3 h to achieve full temperature acclimatization before the aging experiments started.

The cycle aging was performed between 60% and 40% state-of-charge (SOC) with a charge-neutral synthetic hybrid drive cycle [27] (Fig. 1), which was chosen due to its relatively high current throughput. The target voltage, approximately corresponding to 60% SOC, was determined to 3.324 V through galvanostatic intermittent titration technique (GITT) measurements (repeated discharge (C/20; 0.44 A m^{-2}) for 30 min followed by a 3 h open circuit potential (OCP) condition until the lower cutoff voltage of 2.5 V was reached). To correct for SOC slippage, the voltage was potentiostatically readjusted to the 60% SOC target voltage for 10 min after every 20th cycle. The cycle-aged cells were considered

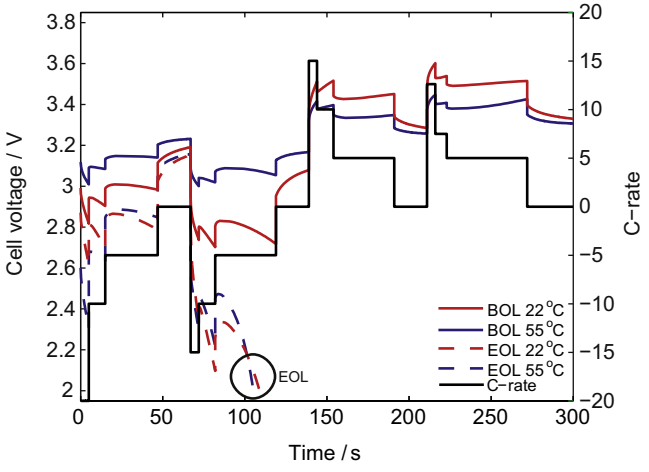

Fig. 1. First hybrid cycle (BOL; solid line) compared to the last cycle (EOL; dashed line), for cells cycled at 22 °C (red) and 55 °C (blue). *Y*-axis to the right: C-rate; *y*-axis to the left: cell voltage response. (For interpretation of the references to colour in this figure legend, the reader is referred to the web version of this article.)

to have reached EOL when either less than 50% of the 1C-discharge capacity at BOL remained or the hybrid cycle no longer could be completed within the specified voltage limits (2.0–3.8 V). The calendar-aged cells were aged for as long as the cycle-aged samples and fixed (potentiostatically) at 60% SOC, except during the reference performance tests (RPTs).

Reference performance tests were performed on the calendar and cycle-aged cells at BOL (after formation cycling), each time the cycle-aged cells had completed another 500 cycles, and at EOL. For the cells aged at 55 °C, the RPTs were repeated at 22 °C at EOL to evaluate the performance. All cells, both calendar and cycle-aged, were left at 60% SOC at EOL prior to disassembly. The RPTs included 1C-discharge capacity determination as well as impedance measurements. The 1C-discharge capacity was measured after a constant current–constant voltage charge routine (CCCV), where the cell was charged galvanostatically to 3.8 V with 1C (8.8 A m^{-2}) and then kept potentiostatically at 3.8 V until the current dropped below 0.35 A m^{-2} (C/25). The cell was then discharged to 2.5 V with 1C. The electrochemical impedance was measured potentiostatically at 60% SOC with 10 mV rms amplitude between 100 kHz and 5 mHz.

In addition to the aged cells, a set of cells were assembled and short-term cycled to serve as a reference for the cycle-aging study. The reference-cycled cells were placed in an oil bath for 3 h at either 22 °C or 55 °C and then cycled for six formation cycles (C/10; 0.88 A m^{-2}), ending with a discharge to 60% SOC.

2.3. X-ray photoelectron spectroscopy characterization

To prepare for X-ray photoelectron spectroscopy measurements, cells were opened inside an argon filled glove box (<1 ppm H_2O) and subsequently transferred, without intermediate exposure to air using a specially built, rubber gasket sealed transfer cup to the vacuum in the spectrometer. Samples were left for 1–2 h in vacuum before the measurement started to allow the pressure to decrease to $<10^{-6}$ mbar. The measurements were performed at a Perkin Elmer PHI 5500 system using the monochromatized 1486.7 eV Al Kα X-ray source. The sample was oriented at an angle of 45° with respect to the analyzer. To avoid radiation damage, the measurement time was kept as short as possible while still discerning the shape of the spectra. No charge neutralization was applied. No charging was observed on the positive electrode. The negative electrode spectra were energy calibrated using the lowest binding energy 284.4 eV peak assigned to C–H/C–C bonds. Curve fits were performed using 30% Lorentzian and 70% Gaussian peak shapes; the lithiated graphite peak was also convoluted with an asymmetric Gelius peak shape. The Gelius peak shape parameters (0.4, 0.38, 20) were taken from the CASA reference library [28] and were found to fit well to C1s spectra of pure graphite powder acquired in our lab. Scofield cross sections [29] were used to determine the relative intensities of different elements. Spectra were normalized to show the relative amounts of the different elements detected in the sample surface, i.e. spectra were divided by spectrum area and multiplied by the relative amount of the element. The relative amounts are here defined as the relative Scofield cross section [29], σ, and polyethylene inelastic mean free path (IMFP) [30], λ, normalized signals, A_j, of the different elements in the sample, as described by equation (1).

$$c_j = \frac{A_j/(\sigma_j \cdot \lambda_j)}{\sum_i A_i/(\sigma_i \cdot \lambda_i)} \quad (1)$$

The differences in the transmission function of the analyzer are negligible at the energies used in the present investigation. In the case of the positive electrode, the iron and lithium contributions were excluded because of uncertainties due to overlap between the Fe2p and Fe3p core level spectra and the fluorine plasmon and Li1s contributions, respectively. Also hydrogen was excluded from the analysis as hydrogen cannot be detected by XPS.

3. Results and discussion

3.1. Full-cell aging

Figs. 2 and 3 show the capacity evolution of cells cycle-aged at 22 °C and 55 °C, respectively. The 22 °C cells reached EOL after 14,000 cycles (115 days including RPTs) while at 55 °C cells lasted for 3000 cycles (25 days including RPTs). Cell lifetime was thus almost five times longer for cells cycled at 22 °C than for cells cycled at 55 °C.

The capacity loss at EOL was fairly similar for cells cycle-aged at 22 °C and 55 °C: 44% and 49%, respectively. At 55 °C, calendar and cycle-aged cells showed similar capacity loss. At 22 °C, the capacity loss of calendar and cycle-aged cells was more different. That is, at ambient temperature, cycling induced processes appear to dominate cell capacity losses while the contribution from cycling related

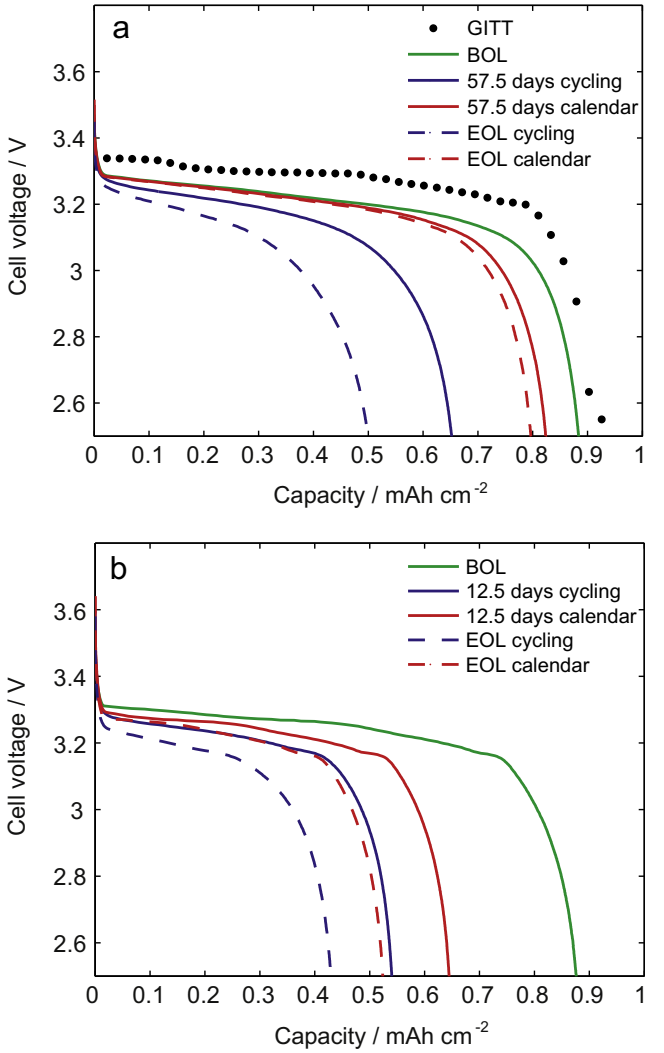

Fig. 2. 1-C discharge capacity at a) BOL, after 57.5 days (7000 cycles) and EOL at 22 °C together with the GITT measurement, b) BOL, after 12.5 days (1500 cycles) and EOL at 55 °C for both cycle- and calendar-aged cells.

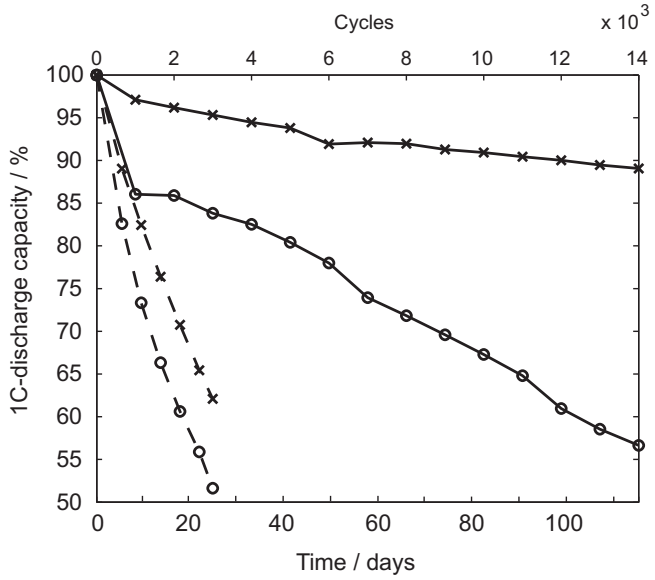

Fig. 3. Capacity retention over time for cycle- (○) and calendar-aged (×) cells at 22 °C (solid lines) and 55 °C (dashed lines).

capacity loss processes appears to be much less pronounced at 55 °C.

In the present work, EOL was defined as when cells had lost either 50% of their initial capacity or their ability to complete the synthetic hybrid drive cycle within the specified voltage window. At both 22 °C and 55 °C, cells failed due to the second criterion that is due to inability to sustain the high rates in the hybrid drive cycle within the specified voltage window. This can be attributed to increased polarization, as seen in Fig. 1.

To investigate the cell impedance development with aging, impedance spectroscopy measurements were performed. The ambient temperature impedance development of cells aged at 22 °C and 55 °C is illustrated in Fig. 4a and b, respectively. Colored frequency markers show the position of 1000, 1 and 0.01 Hz in the different spectra. The 22 °C cycle-aged spectrum shows a changed high-frequency semi-circle shape which has become more elongated and depressed, but the magnitude and position of the curve is similar to the BOL measurements. The 22 °C calendar-aged cell impedance spectra are very similar to BOL spectra. Cells cycle- and calendar-aged at 55 °C show an increased number of semi-circles as well as changes in the slope of the diffusion tail. The position of the 1000 and 1 Hz frequency markers in the inset in Fig. 4b have become shifted along the real axis compared to BOL and the 0.01 Hz markers show a substantial change in the imaginary impedance. The changes in the high and mid-frequency area can be interpreted as resistance and capacitance changes in different parts of the cell, while the changes seen at low frequency might be interpreted as differences in mass transport in the active electrode material and electrolyte. In two parallel studies [23,24], electrodes harvested from the cells aged in this study have been investigated further using a combination of scanning electron microscopy, three-electrode measurements (EIS and cycling) and physics-based EIS models to elucidate the causes of aging. From the study on the harvested electrodes aged at 22 °C the following results were found [23]: calendar aging caused negligible degradation on the positive and negative electrodes, while the positive electrode was the main contributor to the impedance increase for the cycle-aged cells. This impedance increase was mainly attributed to impeded mass transport through the porous structure and loss of active material in the positive electrode.

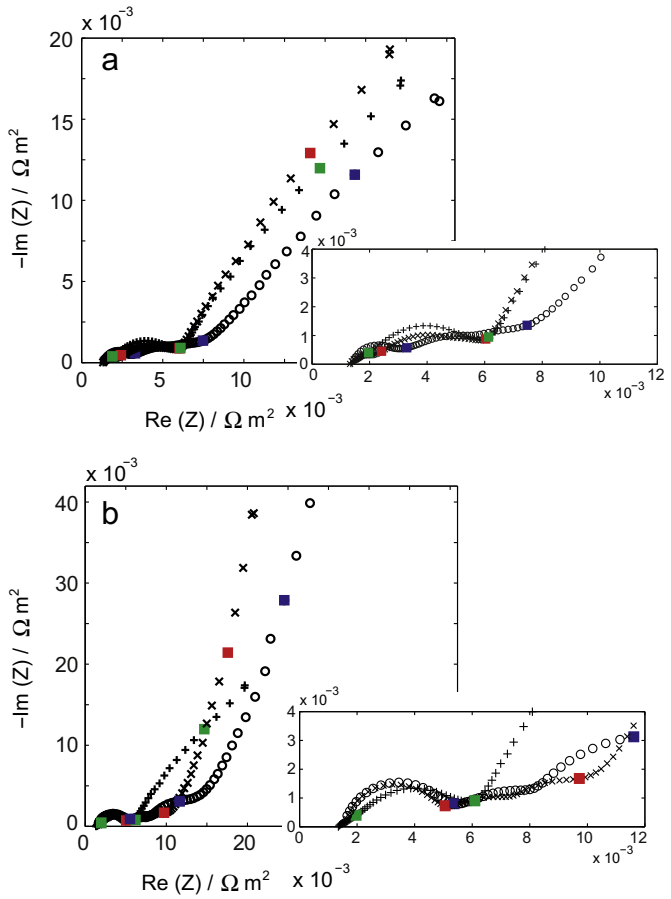

Fig. 4. Electrochemical impedance spectroscopy measured at BOL (+) and EOL for cycle- (○) and calendar-aged (×) cells at a) 22 °C and b) 55 °C. Inset: magnification of the high-frequency area. Notations: green, blue and red squares (□) denotes frequencies 1000, 1 and 0.01 Hz for BOL, cycle- and calendar-aged cells, respectively. (For interpretation of the references to colour in this figure legend, the reader is referred to the web version of this article.)

To gain further insight into the changes in full-cell impedance during cycle aging, the 5 s 20C-discharge step in the beginning of the synthetic hybrid drive cycle was used. These data compliment the impedance spectroscopy data also in the sense that they also demonstrate the resistance evolution at 22 °C and 55 °C, while the impedance spectra were acquired at room temperature for cells cycle-aged at both temperatures. As described in detail elsewhere [31], a current pulse resistance can, similar to impedance spectroscopy, be divided into two different contributions:

- The instantaneous voltage drop related to contact resistances, activation polarization and ohmic potential drop in the electrolyte i.e. ohmic losses.
- The voltage changes during the pulse, related to diffusion polarization in the electrolyte and active electrode material.

The separation of these contributions from a current pulse is illustrated in Fig. 5. Fig. 6a and b shows the absolute resistance increase for the cycled cells. The discharge resistances were normalized by the BOL resistance at the respective temperature to emphasize the trends in resistance increase. The impact of the different BOL resistances on the synthetic hybrid drive cycle at the two temperatures can be seen in Fig. 1. The total increase in the discharge resistance is most pronounced at 55 °C, and dominated by ohmic losses. At 22 °C, similar contributions from time-

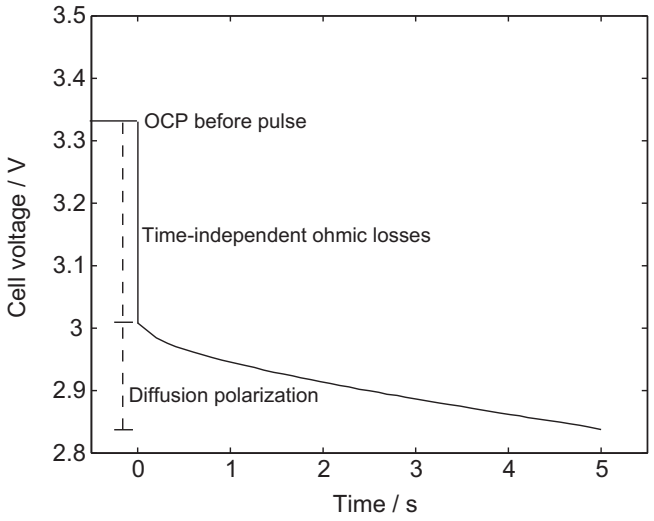

Fig. 5. Illustration of the separation of a discharge pulse into different contributions.

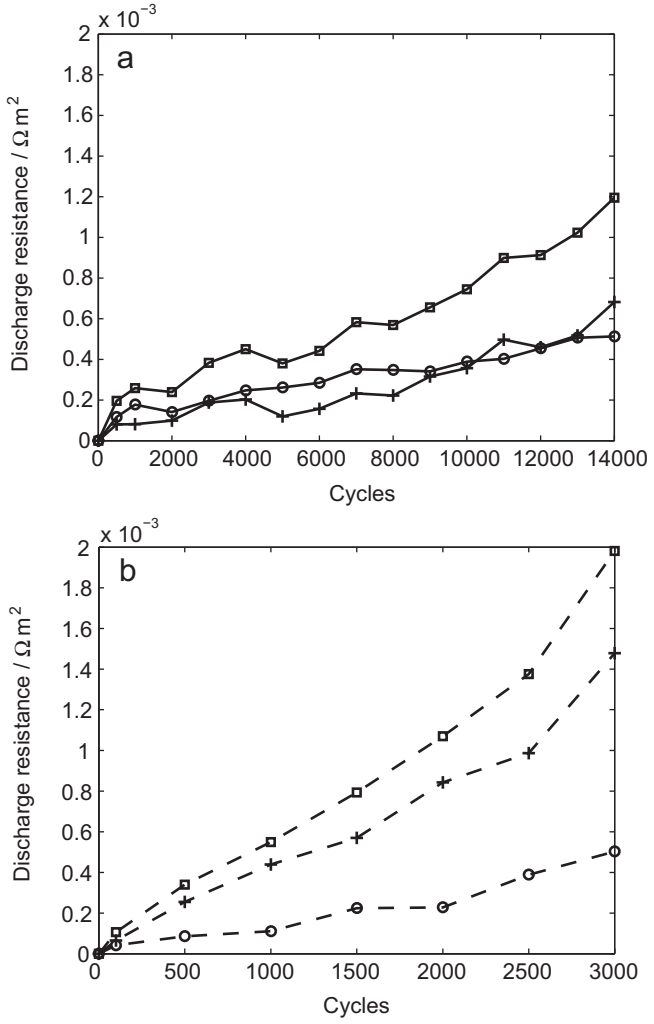

Fig. 6. Absolute increase of discharge resistance compared to BOL for cells cycle-aged at a) 22 °C, b) 55 °C. Notations: total resistance (□), time-independent ohmic losses (+), and diffusion polarization in the electrolyte and active material (○).

independent ohmic losses and the diffusion polarization to the increase of total discharge resistance are seen. However, it is important to consider the effect of the different measurement temperatures between the two methods when comparing the results. The more pronounced losses at 55 °C seen in the current pulse resistance data would have been even more substantial if performed at ambient temperature, as the impedance spectroscopy measurements were. Interestingly, the current pulse resistance data for both temperatures show, like the impedance, that the diffusion polarization increases during prolonged cycling, indicating changes in electrode pore shape and size. Changes in pore morphology in the electrodes and separator also affect the effective conductivity and may thus influence the time-independent losses as well.

To sum up, it can be concluded that cells cycle-aged at 22 °C and 55 °C failed due to increased polarization. Cycle aging at 22 °C and 55 °C affect the cell impedance in different ways. Aging at 22 °C appears to be more related to cycling than aging at 55 °C. At both temperatures changes in diffusion polarization, which could be attributed to changes in pore shape and size, were seen.

3.2. Electrode/electrolyte interface compositions

To further investigate the differences between cells cycle- and calendar-aged to EOL at 22 °C and 55 °C, X-ray photoelectron spectroscopy studies of electrolyte decomposition products and residuals deposited at the electrode/electrolyte interfaces were performed.

3.2.1. Cycle-aged negative electrodes

XPS spectra of negative electrodes from cells cycle-aged to EOL at 22 °C and 55 °C, respectively, are compared in Fig. 7. The spectra are normalized to show the relative amounts of the different elements detected in the sample surface, as described in the Experimental section. Spectra of electrodes from a 55 °C reference-cycled cell (6 cycles at C/10) are shown in Fig. 8 as a baseline for the aging study. Binding energy assignments for the different curve-fitted peaks are summarized in Table 2.

Some interesting differences are shown in the spectra of the 22 °C and 55 °C cycle-aged negative electrode samples. One important difference can be observed in the P2p spectra displayed in Fig. 7. The relative amount of P–O compounds (133.6-8 eV) is considerably larger for the sample cycle-aged at 55 °C compared to at 22 °C. In comparison, the spectra for the 55 °C reference-cycled cells (Fig. 8) show a relatively low P–O contribution. There is, hence, a clear difference not only related to temperature but also to cycling time between samples cycle-aged at 22 °C and 55 °C, respectively. However, the temperature also makes a difference, the growth of the P–O feature is more pronounced in samples cycle-aged at elevated temperature. This can be explained by decomposition of the $LiPF_6$ salt during cycling [32].

In F1s spectra, the sample cycle-aged at 55 °C show a larger relative amount of LiF (684.5-7 eV) than the sample cycled at 22 °C (Fig. 7). This is again in agreement with a possible increased $LiPF_6$ decomposition at elevated temperature, which could be connected to the increased P–O contribution to the P2p spectrum of the elevated temperature cycle-aged sample. The relative amounts of P–F species (136.3-5 eV) in samples cycle-aged at the two temperatures are similar.

The O1s spectra in Fig. 7 exhibit some differences in the relative contributions from different oxygen containing species. The 55 °C cycle-aged sample appears to contain less carbonates (289.9–290.2 eV, labeled CO_3) compared to singly bonded oxygen (533.2-4 eV, labeled C–O). The oxygen speciation in the 22 °C cycle-aged sample seems similar to the 55 °C reference-cycled sample

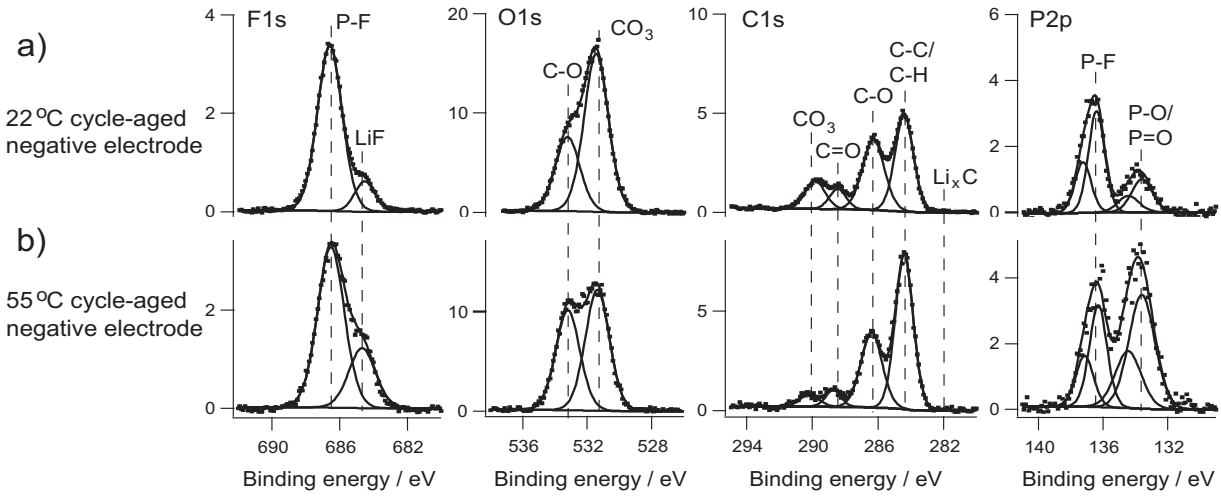

Fig. 7. XPS spectra of cycle-aged negative electrodes at a) 22 °C and b) 55 °C. The spectra are normalized to show the relative amounts of the different elements detected in the sample surface.

(Fig. 8). The differences between cells cycle-aged at the two temperatures can be related to increased oxygenation of $LiPF_6$ decomposition products.

In C1s spectra, the C═O (288.4 eV) feature is more pronounced compared to CO_3/binder (289.9–290 eV) in samples cycled-aged at 55 °C compared to 22 °C (Fig. 7). The C═O feature is significantly less pronounced in the reference-cycled sample spectrum (Fig. 8). Furthermore, the C–C/C–H feature (284.4 eV) is, in Fig. 7, more pronounced in the elevated temperature cycle-aged sample spectra. The graphite feature (282.0 eV) is visible in the reference-cycled sample spectra (Fig. 8), but neither in the 22 °C nor the 55 °C cycle-aged sample spectra (Fig. 7). This indicates that increased amounts of electrolyte products are deposited onto the electrode during cycle aging, or in other words that the SEI thickness increases. However, the probing depth of the XPS measurements is insufficient to investigate possible differences in the SEI thicknesses on samples from cells cycle-aged at different temperatures.

3.2.2. *Cycle-aged positive electrodes*

XPS spectra of positive electrodes harvested from cells cycle-aged to EOL at 22 °C and 55 °C, respectively, are compared in Fig. 9. The spectra are normalized to show the relative amounts of the different elements detected in the sample surface, as described in the Experimental section. Binding energy assignments for the different curve-fitted peaks are summarized in Table 2. For comparison, spectra of a positive electrode reference cycled at 55 °C are also included in Fig. 10 as a baseline for the aging study.

There are some interesting differences in the positive electrode spectra between cells cycle-aged at 22 °C and 55 °C. The trends are, in several cases, similar to the trends seen in the negative electrode/electrolyte interface spectra.

In the P2p spectra, the contribution from P–O compounds (133.2-4 eV) is more pronounced in case of the 55 °C than the 22 °C cycle-aged electrodes. In the O1s spectra, the C–O (533.3-6 eV) contribution is more pronounced for the sample cycle-aged at elevated temperature. The similarities between the P2p and O1s spectra of the negative electrode (Fig. 7) and the positive electrodes (Fig. 9) are striking. However, there is one important difference in the P2p spectrum of the reference-cycled positive electrode (Fig. 10) which differs significantly from that of the reference-cycled negative electrode (Fig. 8) due to the contribution from the phosphate in $LiFePO_4$ (133.3 eV, labeled PO_4).

The similarities between the cycle-aged negative and positive electrode spectra indicate almost full attenuation of the iron phosphate signal in the cycle-aged positive electrode spectra, i.e. that the amount of electrolyte products deposited onto the cycle-aged positive electrodes is so large that the signal from the phosphate in the $LiFePO_4$ is hardly visible. Furthermore, the similarities can also be interpreted as deposition of similar phosphorous and oxygen containing compounds at both the electrodes during cycle aging.

F1s spectra show no traces of LiF (expected at ~685 eV) in the cycle-aged positive electrode/electrolyte interface (Fig. 9). In comparison, LiF was observed in the F1s spectra of the negative electrode at both temperatures (Figs. 7 and 8) and the reference-cycled

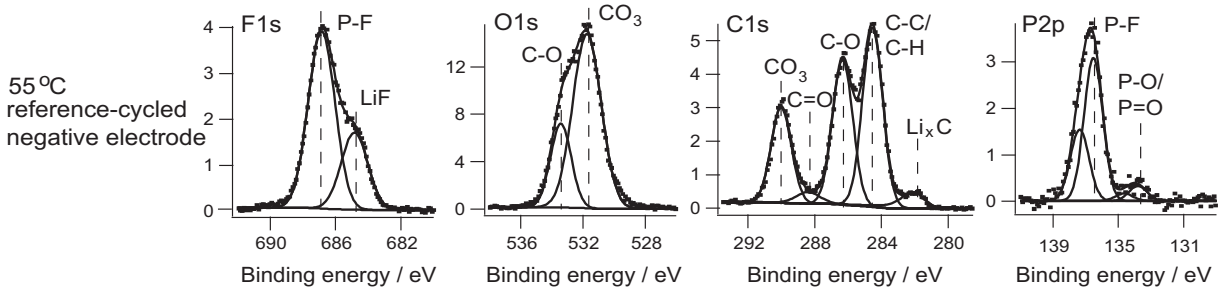

Fig. 8. XPS spectra of a reference-cycled negative electrode (6 cycles at C/10) at 55 °C. The spectra are normalized to show the relative amounts of the different elements detected in the sample surface.

Table 2
Peak assignments of deconvoluted XPS spectra (shown in Fig. 8 for a reference cell cycled at 55 °C).

Element	Bond	Binding energy [eV]
F1s	P–F/binder	686.5-9
	LiF	684.5-8
O1s	C–O	533.1-6
	CO_3/PO_4	531.3-6
C1s	CO_3/binder	289.9–290.4
	C=O	288.4-6
	C–O/binder	285.7–286.4
	C–C/C–H	284.4
	Li_xC	282.0
P2p	P–F	136.0–136.4
	P–O/P=O	133.2–133.7

positive electrode (Fig. 10). In the C1s spectra, there are some differences in the contributions of C–C/C–H (284.4 eV) between samples cycle-aged at the different temperatures (Fig. 9), however the origin of these differences remains unclear.

No Fe2p spectra are included in this work due to overlap with the intense fluorine plasmon. A discussion on the evolution of the iron speciation in aged $LiFePO_4$ electrodes and the amount of iron found on aged graphite electrodes can be found in an XPS study on washed iron phosphate electrodes previously published by Castro et al. [25]. Degradation of $LiFePO_4$ may involve iron dissolution. Iron deposition on the negative electrode has been proposed to catalyze growth of SEI on the negative electrode [33–36]. Interestingly, using X-ray fluorescence (XRF), Castro et al. [25] saw only minor differences between the amounts of iron on negative electrodes from graphite/$LiFePO_4$ cells cycled at room temperature and 60 °C. Hence, they concluded that the amounts of iron in the negative electrodes should not have a major influence on the different rates of capacity loss of cells cycled at the two temperatures.

3.2.3. *Effects of aging scenario on electrolyte decomposition*

The O1s and P2p spectra of cycle-aged negative and positive electrodes (Figs. 7 and 9) are largely similar. Hence, it can be speculated that electrolyte residues dominate the O1s and P2p spectra of the cycle-aged sample. This could be associated with changes in the electrolyte composition during cycling, and increased precipitation of solid material from the electrolyte once it is saturated with some different decomposition products.

In literature, cycling induced formation of oxygenated $LiPF_6$ decomposition products has been suggested to occur through reactions between PF_5, formed on $LiPF_6$ decomposition, and alkoxides forming on diethyl carbonate (DEC) reduction [37].

$$LiPF_6 \rightarrow PF_5 + LiF \quad (2)$$

$$CH_3CH_2OCO_2CH_2CH_3 + e^- + Li^+ \rightarrow CH_3CH_2OLi + CH_3CH_2CO_2 \quad (3)$$

$$PF_5 + CH_3CH_2OLi \rightarrow POF_3 + RF + LiF \quad (4)$$

$$POF_3 + nCH_3CH_2OLi \rightarrow POF_{3-n}(OCH_2CH_3)_n + nLiF \quad (5)$$

Deposition of halophosphates in the pores of the separator, decreasing the electrolyte volume fraction within the separator, has been proposed to account for impedance increase seen in separators harvested from cells cycle-aged at elevated temperature [38]. Similar processes have also been suggested to contribute to the negative and positive electrode impedance rise during aging [16].

If the above reaction scheme would correctly describe the observed changes in electrode/electrolyte interface composition, deposition of P–O containing compounds would be expected to be strongly enhanced by cycling. To check this, XPS spectra of cells calendar-aged at 55 °C (where cycle-aged samples showed the most extensive oxygenation of $LiPF_6$ decomposition products) were acquired. The results are shown in Fig. 11. In contrast to the cycle-aged samples, the O1s and P2p spectra of calendar-aged negative and positive electrodes are significantly different. The $LiFePO_4$ doublet (~134 eV) is clearly visible in the P2p spectrum of the calendar-aged electrode while the phosphorous–oxygen feature is significantly less intense in the graphite spectrum. These results indicate that oxygenation of $LiPF_6$ decomposition products is indeed largely related to cycling, in agreement with the proposed reaction scheme.

In contrast to the significant differences seen in XPS spectra of cells calendar and cycle-aged at 55 °C, both the capacity loss and the impedance increase of cycle- and calendar-aged cells was similar. These results are most noteworthy and indicate that the cells in spite of differences in the electrolyte decomposition schemes can exhibit similar appearance in electrochemical performance degradation.

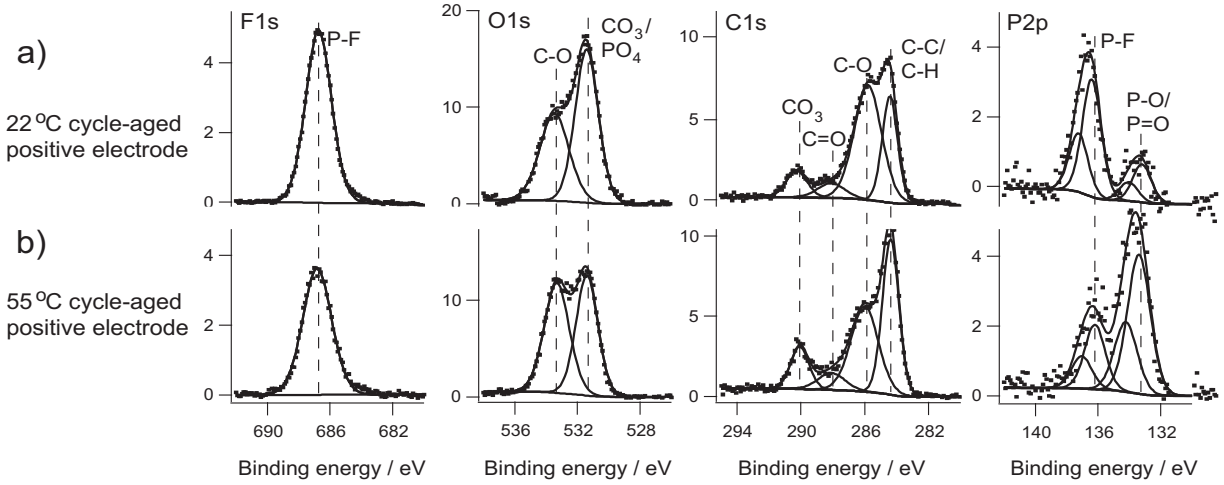

Fig. 9. XPS spectra of cycle-aged positive electrodes at a) 22 °C and b) 55 °C. The spectra are normalized to show the relative amounts of the different elements detected in the sample surface.

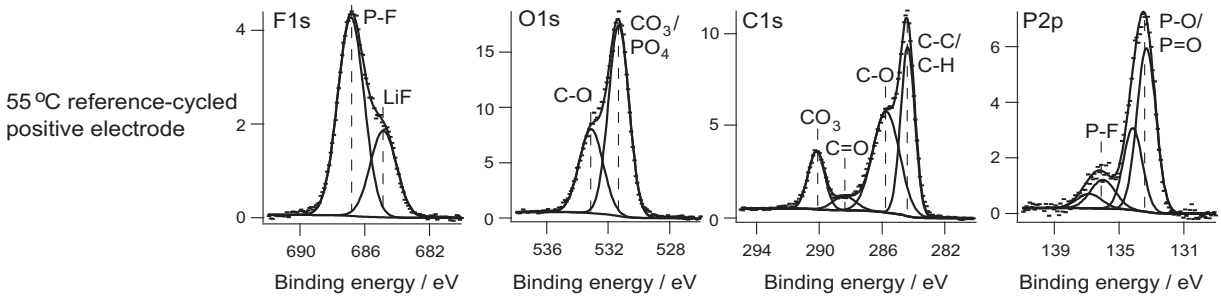

Fig. 10. XPS spectra of a reference-cycled positive electrode at 55 °C. The spectra are normalized to show the relative amounts of the different elements detected in the sample surface.

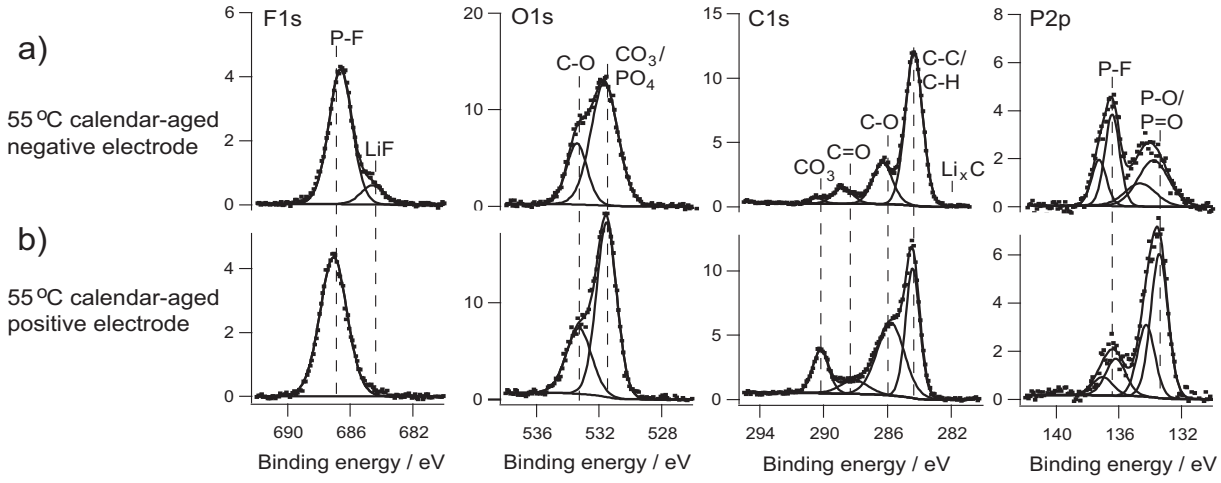

Fig. 11. XPS spectra of calendar-aged a) graphite and b) $LiFePO_4$ electrodes. The spectra were normalized to show the relative amounts of the different elements detected in the sample surface.

As a final remark on electrolyte decomposition, it is noted that the graphite feature (282.0 eV) is no longer visible in the calendar-aged negative electrode spectra (Fig. 11), while it is clearly visible in the reference-cycled sample (Fig. 8). These samples were cycled for similar numbers of cycles (7 and 6.5, respectively) and left at 60% SOC. These results are in agreement with that the SEI thickness increases upon prolonged exposure to elevated temperatures.

The results presented here, based on impedance spectroscopy, battery cycling and XPS, imply that important changes occur in the electrolyte composition during cycle aging. Deposition of electrolyte decomposition compounds in the separator and/or electrode pores could contribute to the diffusion impedance increase implied by the discharge resistance analysis. Deposition of decomposition products from a saturated electrolyte at the electrode/electrolyte interfaces could also contribute to increased ohmic resistance. The compounds that largely precipitate during cycle aging are likely to be more soluble than some other electrode/electrolyte interface compounds, as they appear to largely precipitate at a later stage than many other electrode/electrolyte interface compounds. If so, these studies of non-washed samples have shown to be valuable.

4. Conclusions

The present study compares graphite/$LiFePO_4$-based cells either cycle- or calendar-aged to EOL at 22 °C and 55 °C. In this study, the cause for EOL was, independent of temperature, the inability of the cells to complete a synthetic hybrid drive cycle within the specified voltage limits. Cycling at elevated temperature resulted in a significantly reduced lifetime, almost five times shorter than cells cycled at ambient temperature. The lifetime of calendar-aged cells was also considerably reduced at elevated temperature. Both impedance and discharge-resistance measurements indicated an increase in ohmic losses and diffusion polarizations for the cycle-aged cells, with a dominating effect of the former at elevated temperature.

XPS measurements showed increased formation of oxygenated $LiPF_6$ decomposition products with increased temperature and cycling time. Positive and negative electrodes cycle-aged at the same temperature displayed similarities in XPS spectra, indicating that similar electrolyte products are deposited on both electrodes. Deposition of such electrolyte decomposition products on the electrodes and possibly also in the separator can cause resistive surface films and change the pore shape and size, which could contribute to and explain the changes in impedance and discharge resistance seen in the cycle-aged cell at the two temperatures.

Upon comparison of XPS spectra of cycle- and calendar-aged electrodes at 55 °C some dissimilarities in composition was found, indicating that cycling largely promotes electrolyte decomposition during aging. This is most noteworthy, since, at elevated temperature, cycle- and calendar-aged cells displayed large similarities in capacity loss and impedance increase with aging, which indicates that different electrolyte decomposition processes can result in similar appearance in electrochemical performance degradation.

To conclude, aging at elevated temperature accelerates different aging processes to different extents: the degradation processes are accelerated in process-specific ways. These differences can be important to bear in mind when designing aging tests.

Acknowledgments

This work was conducted as part of the project "Safe and Reliable Battery Systems for Environmental Friendly Vehicles – Development and Test Methods". The financial support from the Swedish Energy Agency, within the framework of FFI program Energy & Environment, and the SHC – Swedish Hybrid Vehicle Centre are gratefully acknowledged. Quallion LLC is also gratefully acknowledged for supplying the electrodes used in this study.

References

[1] R.F. Nelson, Journal of Power Sources 91 (2000) 2–26.
[2] T. Inl, Battery Test Manual for Plug-In Hybrid Electric Vehicles (2010).
[3] J. Vetter, P. Novak, M.R. Wagner, C. Veit, K.C. Moller, J.O. Besenhard, M. Winter, M. Wohlfahrt-Mehrens, C. Vogler, A. Hammouche, Journal of Power Sources 147 (2005) 269–281.
[4] P. Liu, J. Wang, J. Hicks-Garner, E. Sherman, S. Soukiazian, M. Verbrugge, H. Tataria, J. Musser, P. Finamore, Journal of the Electrochemical Society 157 (2010) A499–A507.
[5] J. Wang, P. Liu, J. Hicks-Garner, E. Sherman, S. Soukiazian, M. Verbrugge, H. Tataria, J. Musser, P. Finamore, Journal of Power Sources 196 (2011) 3942–3948.
[6] M. Safari, C. Delacourt, Journal of the Electrochemical Society 158 (2011) A1123–A1135.
[7] M. Dubarry, B.Y. Liaw, Journal of Power Sources 194 (2009) 541–549.
[8] M. Kassem, J. Bernard, R. Revel, S. Pelissier, F. Duclaud, C. Delacourt, Journal of Power Sources 208 (2012) 296–305.
[9] J. Shim, K.A. Striebel, Journal of Power Sources 119 (2003) 955–958.
[10] K. Striebel, J. Shim, A. Sierra, H. Yang, X.Y. Song, R. Kostecki, K. McCarthy, Journal of Power Sources 146 (2005) 33–38.
[11] H. Zheng, L. Chai, X. Song, V. Battaglia, Electrochimica Acta 62 (2012) 256–262.
[12] K. Striebel, A. Guerfi, J. Shim, M. Armand, M. Gauthier, K. Zaghib, Journal of Power Sources 119 (2003) 951–954.
[13] J. Wang, S. Soukiazian, M. Verbrugge, H. Tataria, D. Coates, D. Hall, P. Liu, Journal of Power Sources 196 (2011) 5966–5969.
[14] M. Maccario, L. Croguennec, F. Le Cras, C. Delmas, Journal of Power Sources 183 (2008) 411–417.
[15] D.Y. Wang, X.D. Wu, Z.X. Wang, L.Q. Chen, Journal of Power Sources 140 (2005) 125–128.
[16] M. Dubarry, B.Y. Liaw, M.-S. Chen, S.-S. Chyan, K.-C. Han, W.-T. Sie, S.-H. Wu, Journal of Power Sources 196 (2011) 3420–3425.
[17] R. Kostecki, L. Norin, X.Y. Song, F. McLarnon, Journal of the Electrochemical Society 151 (2004) A522–A526.
[18] S. Brown, K. Ogawa, Y. Kumeuchi, S. Enomoto, M. Uno, H. Saito, Y. Sone, D. Abraham, G. Lindbergh, Journal of Power Sources 185 (2008) 1444–1453.
[19] W. Waag, S. Käbitz, D.U. Sauer, Applied Energy 102 (2013) 885–897.
[20] Y. Zhang, C.-Y. Wang, X. Tang, Journal of Power Sources 196 (2011) 1513–1520.
[21] N. Mellgren, S. Brown, M. Vynnycky, G. Lindbergh, Journal of the Electrochemical Society 155 (2008) A304–A319.
[22] S. Brown, N. Mellgren, M. Vynnycky, G. Lindbergh, Journal of the Electrochemical Society 155 (2008) A320–A338.
[23] T.G. Zavalis, M. Klett, M.H. Kjell, M. Behm, R.W. Lindström, G. Lindbergh, Electrochimica Acta (2013), http://dx.doi.org/10.1016/j.electacta.2013.05.081.
[24] M. Klett, T.G. Zavalis, M.H. Kjell, M. Behm, R.W. Lindström, G. Lindbergh, in preparation.
[25] L. Castro, R. Dedryvere, J.B. Ledeuil, J. Breger, C. Tessier, D. Gonbeau, Journal of the Electrochemical Society 159 (2012) A357–A363.
[26] K. Tasaki, A. Goldberg, J.-J. Lian, M. Walker, A. Timmons, S.J. Harris, Journal of the Electrochemical Society 156 (2009) A1019–A1027.
[27] Electrically Propelled Road Vehicles – Test Specifications for Lithium-ion Traction Battery Packs and Systems – Part 1: High-power Applications (2011), p. 26. ISO 12405-1.
[28] M.C. Biesinger, X-ray Photoelectron Spectroscopy Reference Pages (2012). http://xpsfitting.blogspot.com/2008/12/graphite.html.
[29] J.H. Scofield, Theoretical Photoionization Cross Sections from 1 to 1500 keV Lawrence L (1973). UCRL-51326.
[30] L.R. Painter, E.T. Arakawa, M.W. Williams, J.C. Ashley, Radiation Research 83 (1980) 1–18.
[31] A. Nyman, T.G. Zavalis, R. Elger, M. Behm, G. Lindbergh, Journal of the Electrochemical Society 157 (2010) A1236–A1246.
[32] M. Herstedt, D.P. Abraham, J.B. Kerr, K. Edström, Electrochimica Acta 49 (2004) 5097–5110.
[33] H.-C. Wu, C.-Y. Su, D.-T. Shieh, M.-H. Yang, N.-L. Wu, Electrochemical and Solid State Letters 9 (2006) A537–A541.
[34] K. Amine, J. Liu, I. Belharouak, Electrochemistry Communications 7 (2005) 669–673.
[35] M. Koltypin, D. Aurbach, L. Nazar, B. Ellis, Journal of Power Sources 174 (2007) 1241–1250.
[36] N. Dupré, J.-F. Martin, J. Degryse, V. Fernandez, P. Soudan, D. Guyomard, Journal of Power Sources 195 (2010) 7415–7425.
[37] G. Gachot, S. Grugeon, M. Armand, S. Pilard, P. Guenot, J.-M. Tarascon, S. Laruelle, Journal of Power Sources 178 (2008) 409–421.
[38] L. Norin, R. Kostecki, F. McLarnon, Electrochemical and Solid State Letters 5 (2002) A67–A69.